Structure of a sheared soft-disk fluid from a nonequilibrium potential

C. Baig,[1] Yu. V. Kalyuzhnyi,[2] S. T. Cui,[1,3] and H. D. Cochran[1,3]
[1]*Department of Chemical Engineering, University of Tennessee, Knoxville, Tennessee 37996-2200, USA*
[2]*Institute for Condensed Matter Physics, Svientsitskoho 1, 79011 Lviv, Ukraine*
[3]*Chemical Sciences Division, Oak Ridge National Laboratory, Oak Ridge, Tennessee 27831-6110, USA*
(Received 30 July 2004; published 29 December 2004)

The distortion of structure of a simple, inverse-12, soft-disk fluid undergoing two-dimensional plane Couette flow was studied by nonequilibrium molecular dynamics (NEMD) simulation and by equilibrium Monte Carlo (MC) simulation with a nonequilibrium potential, under which the equilibrium structure of the fluid is that of the nonequilibrium fluid. Extension of the iterative predictor-corrector method of [Reatto *et al.*Phys. Rev. A **33** 3451 (1986)] was used to extract the nonequilibrium potential with the structure input from the NEMD simulation. Very good agreement for the structural properties and pressure tensor generated by the NEMD and MC simulation methods was found, thus providing the evidence that nonequilibrium liquid structure can be accurately reproduced via simple equilibrium simulations or theories using a properly chosen nonequilibrium potential. The method developed in the present study and numerical results presented here can be used to guide and test theoretical developments, providing them with the "experimental" results for the nonequilibrium potential.

DOI: 10.1103/PhysRevE.70.061204 PACS number(s): 66.20.+d, 05.20.Jj

I. INTRODUCTION

Shear-induced distortion of the fluid structure and its relation to the rheological properties of the fluid are of substantial importance in a number of applications in many branches of science and engineering. However, there have been only few attempts at a theoretical description of the fluid structure undergoing shear flow. These include phenomenological approaches based on fluctuating hydrodynamics [1–3] and on the Langevin models [4,5]. More recently a relatively successful description of the structural changes in the hard-sphere fluid under shear was given by Lutsko [6], where he combines solution of the Enskog equation [7], which gives the contact value of the hard-sphere pair distribution function, and ideas of the generalized mean spherical approximation approach [8].

An interesting prospect in developing the theory, which is able to describe shear-induced distortion of the fluid structure, is to use the well-developed machinery of the liquid-state equilibrium statistical mechanics with a nonequilibrium potential under which the equilibrium structure of a fluid is that of the nonequilibrium fluid. Such theory can be used to predict the structure and other properties of nonequilibrium fluids without utilizing computer simulation methods. This is especially important for being able to predict the properties of the system under conditions at which they cannot be determind by computer simulation, e.g., in the linear flow regime of high polymers or in uniaxial extensional flow in the nonlinear regime. This type of approach has been taken by Gan and Eu [9,10]; however extensive comparison of the theoretical results and results of nonequilibrium molecular dynamics (NEMD) simulation [11,12] reveals poor performance of the nonequilibrium potential suggested by the authors.

In this paper we continue to explore the possibilities in suggesting the nonequilibrium potential, which can be used to predict shear-induced distortion of the fluid structure. Calculation of the nonequilibrium potential represents a crucial step in the theory discussed above and availability of the "exact" results is very important, since they can be used as a reference to test the theory. While formal existence of the nonequilibrium potential follows from considerations of Gan and Eu [9,10], knowledge of its quantitative and even qualitative form is still lacking. Moreover, there is no evidence that the nonequilibrium potential can be determined or of the conditions of the density and strain rate under which it can be determined with sufficient accuracy. In the present study we propose a scheme, which gives "exact" results for the nonequilibrium potential in the same sense as any computer simulation approach gives "exact" results for the liquid structure. Our scheme combines NEMD and Monte Carlo simulation methods with the iterative predictor-corrector method of Reatto *et al.* [17]. The NEMD simulation method is used to generate the pair distribution function of the fluid undergoing steady shear flow, and the MC method is a "corrector" step in the predictor-corrector method of Reatto *et al.* [17]. In essence, the scheme represents solution of the inverse problem for the structure generated by the NEMD simulations. This method can be used to guide theoretical developments providing them with the "experimental" results for the nonequilibrium potential, which otherwise are not available.

The paper is organized as follows. In the next section we present the model and details of the NEMD simulation. For the sake of simulation simplicity we consider here the inverse-12, soft-disk fluid undergoing two-dimensional plane Couette flow. In Sec. III we discuss the iterative predictor-corrector method of Reatto *et al.* [17], specialized to the problem at hand; in Sec. IV we present our results and discussion; and in Sec. V we collect our conclusions. In addition, in the Appendix we propose a closed-form, analytic expression for the nonequilibrium potential, extracted from the NEMD simulation, and its parametrization.

II. NONEQUILIBRIUM MOLECULAR DYNAMICS SIMULATIONS

Canonical (NVT) NEMD simulations of the soft-disk fluid under a planar Couette shear field have been performed using the so-called Sllod equations of motion [13] with a Nose-Hoover thermostat [14–16]. The interaction potential of the soft-disk fluid is given by

$$V_{eq}(r) = \epsilon\left(\frac{\sigma}{r}\right)^{12}. \tag{1}$$

The interaction force and potential are truncated at $r = 2.0\sigma$. In this study, we have chosen the reduced temperature $T^* = k_B T/\epsilon = 1.0$ and three different packing fractions $\eta = \pi\rho\sigma^2/4 = 0.3$, 0.35, and 0.4. Three different values of the reduced shear rates $\gamma^* = \gamma\sqrt{m\sigma^2/\epsilon} = 0.5$, 0.7, and 1.0 were used. All NEMD simulations have been carried with 2048 soft disks. The velocity Verlet algorithm was employed to integrate the equations of motion with the reduced time step $\delta t^* = \delta t/\sqrt{m\sigma^2/\epsilon} = 0.001$. A total of 10 million time steps was used for every NEMD simulation, which is sufficient to reduce the statistical uncertainty. For calculating $g(\mathbf{r})$ during simulations, two-dimensional space has been divided by $\delta r = 0.01\sigma$ and $\delta\theta = 2\pi/1000$. A small grid in the angular coordinate was required for the inversion procedure to extract the nonequilibrium potentials. After 2 million time steps to achieve steady state, $g(\mathbf{r})$ data were collected every 10 steps.

III. NONEQUILIBRIUM POTENTIAL AND EQUILIBRIUM MONTE CARLO SIMULATIONS

A. Solution of the inverse problem

According to liquid state integral equation theory, formal solution of the inverse problem, i.e., deduction of the interparticle interaction potential $V_{ne}(\mathbf{r})$ from the structural data, is

$$\beta V_{ne}(\mathbf{r}) = t(\mathbf{r}) + B(\mathbf{r}) - \ln[g(\mathbf{r})], \tag{2}$$

where $g(\mathbf{r}) = h(\mathbf{r}) + 1$, $t(\mathbf{r}) = h(\mathbf{r}) - c(\mathbf{r})$, $B(\mathbf{r})$ is the so-called bridge function, and the total $h(\mathbf{r})$ and direct $c(\mathbf{r})$ correlation functions are coupled by the Ornstein-Zernike (OZ) equation

$$h(\mathbf{r}_{12}) = c(\mathbf{r}_{12}) + \rho\int d\mathbf{r}_3 c(\mathbf{r}_{13})h(\mathbf{r}_{32}). \tag{3}$$

However, this set of equations is not closed and one has to adopt some approximation for the bridge function $B(\mathbf{r})$. The resulting potential is very sensitive to the accuracy of the approximation used, which makes solution of the inverse problem highly nontrivial. One of the possibilities in resolving the problem is to utilize an iterative solution method, correcting the initial approximation to the bridge function [or equivalently to the potential $V_{ne}(\mathbf{r})$ (2)] on each iterative step.

In this study we utilize the iterative predictor-corrector method of Reatto *et al.* [17], which proves to be successful in a number of applications. One iterative cycle of this method combines a "corrector" step, represented by the full computer simulation for the pair potential obtained on a "predictor" step using expression (2). On the ith iteration cycle we have

$$\beta V_{ne}^{(i)}(\mathbf{r}) = \beta V_{ne}^{(i-1)}(\mathbf{r}) + t_{NEMD}(\mathbf{r}) - t^{(i-1)}(\mathbf{r}) - \ln[g_{NEMD}(\mathbf{r})] + \ln[g^{(i-1)}(\mathbf{r})], \tag{4}$$

where the subscript NEMD denotes the quantities obtained by the NEMD simulation and correlation functions $t^{(i-1)}(\mathbf{r})$ and $h^{(i-1)}(\mathbf{r})$ for $i-1$ iteration step follow from the equilibrium MC simulation method applied to the system with the pair potential $V_{ne}^{(i-1)}(\mathbf{r})$.

The inversion scheme of this type requires a very accurate initial guess for the pair potential $V_{ne}(\mathbf{r})$. In the present study we used the following initial estimate,

$$V_{ne}^{(0)}(\mathbf{r}) = t_{NEMD}(\mathbf{r}) - \ln[g_{NEMD}(\mathbf{r})] + B^{(0)}(\mathbf{r}), \tag{5}$$

where $B^{(0)}(\mathbf{r})$ is the bridge function extracted from the equilibrium MC simulations for the original system in equilibrium ($\gamma^* = 0$) with the pair potential (1).

Application of the iteration scheme (4) requires solution of the OZ equation (3) with respect to $t(\mathbf{r})$, i.e.,

$$t(\mathbf{r}_{12}) = \rho\int d\mathbf{r}_3[h(\mathbf{r}_{13}) - t(\mathbf{r}_{13})]h(\mathbf{r}_{32}). \tag{6}$$

The integral equation given by (6) involves correlation functions, which are vector dependent and therefore difficult to solve numerically. To overcome this difficulty we expand these correlation functions into a set of ortogonal functions [18], i.e.,

$$S(r,\theta) = \sum_{m=-L}^{L} S_m(r)\exp(im\theta), \tag{7}$$

which reduces the problem to numerically solving the one-variable function $S_m(r)$. Here $S(r,\theta)$ stands for either $t(r,\theta)$ or $h(r,\theta)$ and $L\to\infty$. Taking the Fourier transform of the OZ Eq. (3) and expanding the correlation functions $\hat{t}(\mathbf{k})$ and $\hat{h}(\mathbf{k})$, we have

$$\hat{t}_m(k) = \rho\sum_{p=-L}^{L}[\hat{h}_m(k) - \hat{t}_p(k)]\hat{h}_{m-p}(k), \tag{8}$$

where the expansion coefficients in real and Fourier spaces are linked by the relation

$$\hat{S}_m(k) = 2\pi i^m\int_0^\infty dr r S_m(r)J_m(kr). \tag{9}$$

Here J_p denotes the pth order Bessel function of the first kind.

It is convenient to write Eq. (8) in matrix form, which then can be solved for $\hat{t}_m(k)$ to yield

$$\hat{\mathbf{t}}(k) = \rho\hat{\mathbf{h}}(k)\hat{\mathbf{H}}(k)[\mathbf{1} + \rho\hat{\mathbf{H}}(k)]^{-1} \tag{10}$$

where $\hat{\mathbf{t}}(k) = (\hat{t}_{-L}(k), \ldots, \hat{t}_L(k))$, $\hat{\mathbf{h}}(k) = (\hat{h}_{-L}(k), \ldots, \hat{h}_L(k))$, and

$$[\hat{\mathbf{H}}(k)]_{nm} = \sum_{p=-L}^{L}\hat{h}_p(k)\,\delta_{p,m-n}. \tag{11}$$

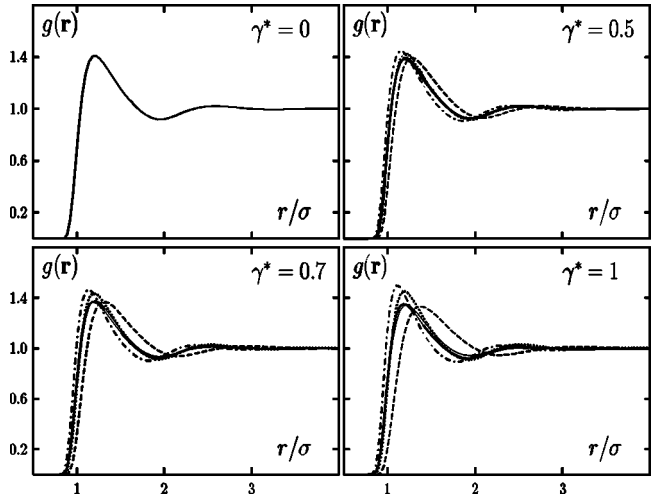

FIG. 1. Pair distribution function $g(\mathbf{r})$ of the soft-disk fluid under shear flow at $\eta=0.3$ and $\theta=0$ (solid lines), $\theta=\pi/4$ (dashed lines), $\theta=\pi/2$ (dotted lines), and $\theta=3\pi/4$ (dashed-dotted lines) at different values of the shear rate γ^* by NEMD simulation. The thin solid line represents $g_0(r)$, which is the orientationally averaged version of the pair distribution function $g(\mathbf{r})$.

Summation in these expressions formally extends from minus to plus infinity ($L\rightarrow\infty$); in most cases only a small number of coefficients are needed. In the present study we restrict ourselves to $L=8$, which appears to be sufficient for good representation of the structure. Because of the symmetry of the problem, all the expansion coefficients $S_m(r)$ and $(\hat{S}(k))$ with odd m are equal zero, and $S_{-m}(r)=[S_m(r)]^*$, where the asterisk denotes complex conjugate. Thus, the dimensionality of the matrices involved in the Eq. (10) is 9×9. The forward and inverse Fourier transforms, which are needed to couple the coefficients of the expansions of the correlation functions, have been carried out in logarithmic variables, using the method developed by Talman [19]. This method allows us to sample effectively both the rapidly varying part of the correlation functions at small distances and the long-range, slowly decaying portion, using a small number of grid points ($n=512$).

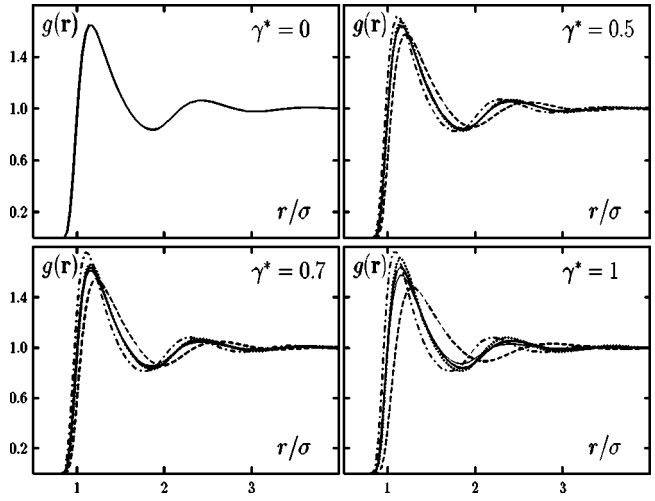

FIG. 2. The same as in Fig. 1 for $\eta=0.4$.

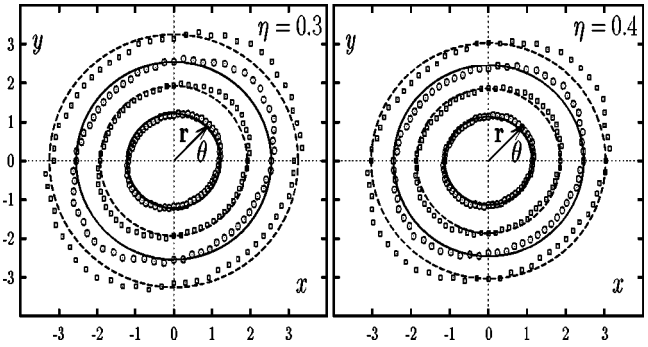

FIG. 3. Location of the pair distribution function maxima (solid lines and circles) and minima (dashed lines and squares) at different values of η and at $\gamma^*=0$ (lines) and $\gamma^*=0.7$ (symbols). All results are from NEMD simulation.

B. Details of the equilibrium Monte Carlo simulations

Each iterative step of the method discussed above requires full Monte Carlo simulation of the equilibrium system with the pair potential $V_{ne}^{(i)}(\mathbf{r})$. Temperature, density, and the equilibrium interaction potential used in MC simulations are the same as those in NEMD simulations. A total of 2 million cycles were performed for every MC simulation. After a 500 000-cycle equilibration, $g(\mathbf{r})$ data were collected every 10 cycles. An important detail in the MC simulations is to use a much larger (shear-rate dependent) cut-off distance than is used in the NEMD simulations because of the long-range characteristic of the nonequilibrium potential. It turns out (see Fig. 5) that the range of the nonequilibrium potential becomes longer with increasing shear rate. For all packing fractions, we employed $r_{cut}=6.0\sigma$ in the case of $\gamma^*=0.5$ and 0.7, and $r_{cut}=8.0\sigma$ in the case of $\gamma^*=1.0$. This strategy was necessary in order to avoid an artificial discontinuity in $g(\mathbf{r})$ at shorter r_{cut}. Moreover, it also turns out that more iterations are required for the higher shear rate.

IV. RESULTS AND DISCUSSION

Figures 1 and 2 show the development of anisotropic structure, $g(\mathbf{r})$, for the system at $\eta=0.3$ and 0.4 at shear rate $\gamma^*=0$, 0.5, 0.7, and 1.0. As expected, for the equilibrium case, $\gamma^*=0$, $g(\mathbf{r})$ reveals no angular dependence, indicating

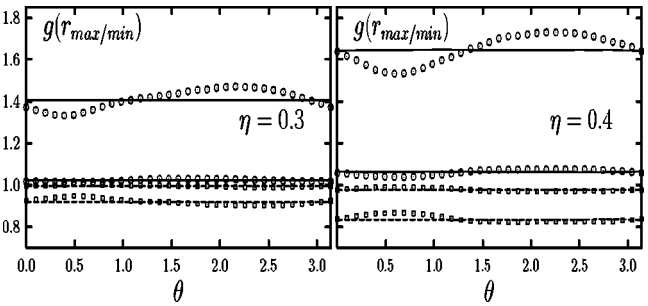

FIG. 4. The values of the pair distribution function maxima (solid lines and circles) and minima (dashed lines and squares) versus θ at different values of η and at $\gamma^*=0$ (lines) and $\gamma^*=0.7$ (symbols). All results are from NEMD simulation.

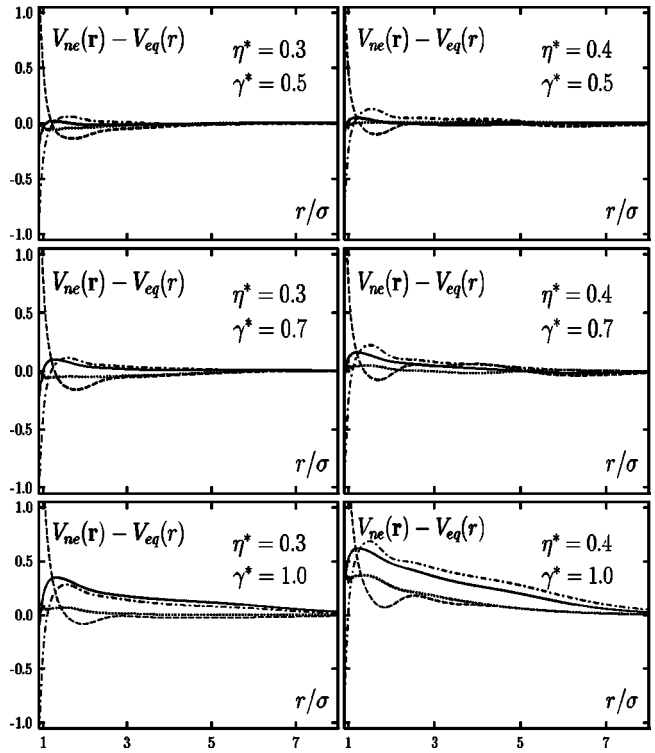

FIG. 5. The difference between nonequilibrium and equilibrium potentials $V_{ne}(\mathbf{r}) - V_{eq}(r)$ at different values of η and γ^* for $\theta = 0$ (solid lines), $\theta = \pi/4$ (dashed lines), $\theta = \pi/2$ (dotted lines), and $\theta = 3\pi/4$ (dashed-dotted lines).

the isotropic nature of liquid structure under the spherically symmetric soft interaction potential (1). For the nonequilibrium case of $\gamma^* = 0.5$, it is clearly seen that the applied shear field distorts the overall liquid structure. Approximately, $g(r, \theta = 0)$ is almost the same as the angle-averaged $g_0(r)$, and on the scale of the figure the difference can be seen only for the case of the largest shear rate $\gamma^* = 1.0$. Physically this

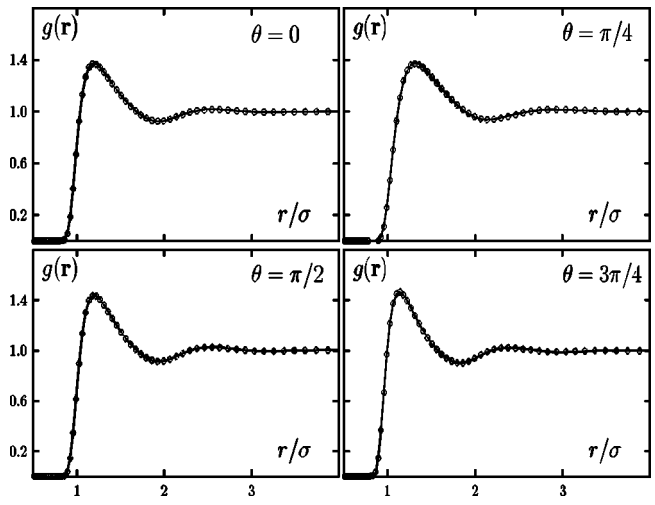

FIG. 6. Comparison of the pair distribution functions obtained by the NEMD simulation with the equilibrium pair potential $V_{eq}(r)$ and by equilibrium MC simulation with the nonequilibrium potential $V_{ne}(\mathbf{r})$ at $\eta = 0.3$ and $\gamma^* = 0.7$ and different values of θ.

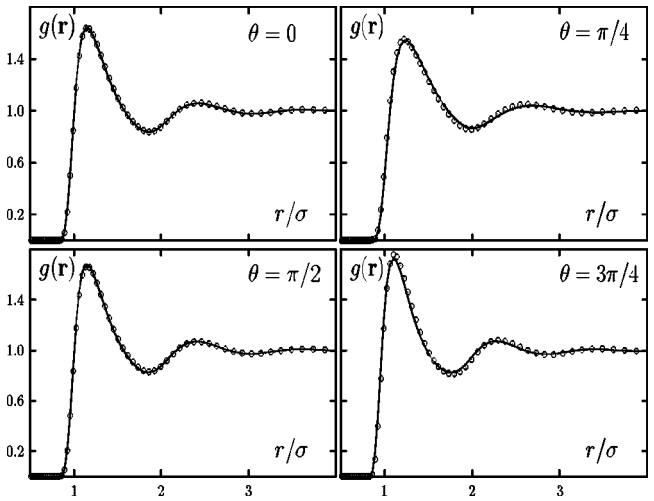

FIG. 7. The same as in Fig. 6 for $\eta = 0.4$.

means that the structural shape of the system at $\theta = 0$ is not much changed by the external shear force. $g(r, \theta = \pi/2)$ also shows little difference from $g_0(r)$ except a slightly higher value of the first maximum. In contrast to those at $\theta = 0$ and $\pi/2$, $g(\mathbf{r})$ at $\theta = \pi/4$ and $3\pi/4$ show quite different results. Relative to $g_0(r)$, $g(r, \theta = \pi/4)$ appears to shift to larger r and $g(r, \theta = 3\pi/4)$ to smaller r. This indicates that particles are distributed in space closer to each other at $\theta = 3\pi/4$, but further apart from each other at $\theta = \pi/4$. In a sense, we can say that particles have stronger interactions with those located in the direction of $\theta = 3\pi/4$ relative to them and weaker interactions with those in the direction of $\theta = \pi/4$. In this regard, it is to be expected from the fundamental kinetic theory that transport coefficients, i.e., viscosity, would be different for different orientations in space under the shear field. It is also important to note that the first maximum peak of $g(\mathbf{r})$ at $\theta = 3\pi/4$ appears considerably higher than that of $g_0(r)$. Combining all the results above, we can picture the overall shape of the liquid structure as an ellipse distorted from a circle with its major axis in the direction of $\theta = \pi/4$. The overall liquid structures at $\gamma^* = 0.7$ and 1.0 appear qualitatively similar to that at $\gamma^* = 0.5$. However, the distortion of liquid structure becomes stronger with increasing shear rate. In both cases, $g(r, \theta = 0)$ still shows little difference from $g_0(r)$ as in the case of $\gamma^* = 0.5$. For $g(r, \theta = \pi/2)$, the maximum value is now considerably higher than that of $g_0(r)$, although there is still no clear shift in the position of the peaks, i.e., the periodicity of peaks. $g(r, \theta = \pi/4)$ and $g(r, \theta = 3\pi/4)$ also show the stronger shear effect on the extent of the shift, while only $g(r, \theta = 3\pi/4)$ shows a clear increase of the maximum value of peak. Thus the resulting shape of structure in these cases is elliptical as in the case of $\gamma^* = 0.5$, but with a higher degree of eccentricity. The exact quantitative picture of the elliptical shape liquid structure is well represented in Fig. 3. Figure 4 shows the maximum and minimum values of $g(\mathbf{r})$ along the angular coordinate. One can see that the most substantial deviation of $g(\mathbf{r})$ extremum values occurs for orientations close to $\theta = \pi/6$ and $\theta = 3\pi/4$, while for $\theta = 0$ $g(\mathbf{r})$ it is almost unchanged.

Our results for the nonequilibrium potential $V_{ne}(\mathbf{r})$ extracted from the NEMD simulation results are presented in

TABLE I. Pressure tensor $\mathbf{P}=(1/\mathbf{V})\Sigma_i^N \mathbf{r}_i\mathbf{f}_i$ calculated using NEMD simulation for equilibrium pair potential $V_{eq}(r)$ and equilibrium MC simulation for nonequilibrium potential $V_{ne}(\mathbf{r})$.

η	γ^*	$P_{xx}^{(NEMD)}$	$P_{xx}^{(MC)}$	$P_{xy}^{(NEMD)}$	$P_{xy}^{(MC)}$	$P_{yy}^{(NEMD)}$	$P_{yy}^{(MC)}$
	0.5	0.4917	0.4913	−0.0798	−0.0802	0.4828	0.4817
0.30	0.7	0.5030	0.5064	−0.1080	−0.1080	0.4898	0.4925
	1.0	0.5219	0.5235	−0.1461	−0.1458	0.5033	0.5027
	0.5	0.7519	0.7513	−0.1135	−0.1121	0.7444	0.7425
0.35	0.7	0.7674	0.7685	−0.1557	−0.1552	0.7557	0.7550
	1.0	0.7941	0.7913	−0.2129	−0.2106	0.7777	0.7743
	0.5	1.1145	1.1139	−0.1600	−0.1589	1.1089	1.1069
0.40	0.7	1.1355	1.1341	−0.2193	−0.2176	1.1275	1.1253
	1.0	1.1732	1.1739	−0.3015	−0.2967	1.1618	1.1637

Fig. 5. In order to see clearly the effect of shear on the liquid structure, it is useful to divide nonequilibrium potential into two parts: equilibrium part, $V_{eq}(r)$, and the purely nonequilibrium part, $V_{ne}(\mathbf{r})-V_{eq}(r)$. Figure 5 plots the purely nonequilibrium part of potential. It is instructive to compare the shape of the nonequilibrium part and $g(\mathbf{r})$ as shown in Figs. 1 and 2. In particular, the shape at $\theta=\pi/4$ looks almost opposite to that at $\theta=3\pi/4$, which is consistent with the results of $g(\mathbf{r},)$. Another aspect worthy of notice is that nonequilibrium potential is relatively long-ranged and its range becomes longer as shear rate increases. Note that this feature is absent in the theory of Gan and Eu [9,10], which predicts the same large distance asymptotic for both equilibrium and nonequilibrium potentials.

Figures 6 and 7 show the results of inversion calculations of $g(\mathbf{r})$ for $\eta=0.3$ and 0.4 at shear rate $\gamma^*=0.7$ by MC simulations with the nonequilibrium potentials that were extracted from the original $g(\mathbf{r})$ data from NEMD simulations. As shown in the figures, the inversion results in all cases converge very well to the original ones. This proves that our nonequilibrium potentials are accurate enough to represent the corresponding nonequilibrium liquid structures. This treatment has an important practical aspect since we can reproduce the structure of a nonequilibrium system via simple equilibrium simulations or theories using a properly chosen nonequilibrium potential. Similarly, good agreement between equilibrium MC and NEMD simulation results was found for

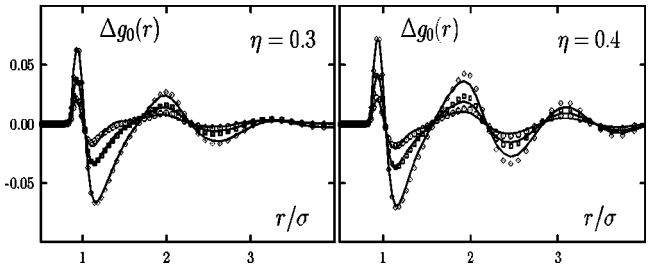

FIG. 8. Comparison of the distortion of the fluid structure $\Delta g_{00}(r)=g_{00}(r)-g_{eq}(r)$ calculated using NEMD simulation with the equilibrium pair potential $V_{eq}(r)$ (symbols) and equilibrium MC simulation with the nonequilibrium potential $V_{ne}(\mathbf{r})$ (solid lines) at different values of η and at $\gamma=0.5$ (circles), $\gamma=0.7$ (squares) and $\gamma=1.0$ (diamonds). Here $g_{00}(r)$ is the angular averaged version of the pair distribution function $g(\mathbf{r})$.

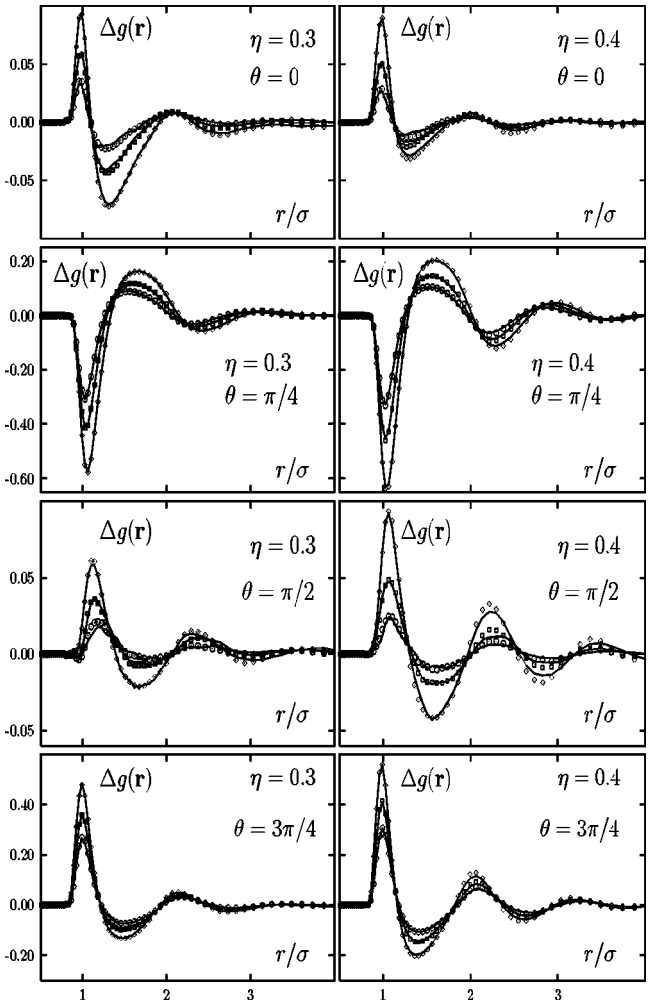

FIG. 9. Comparison of the distortion of the fluid structure $\Delta g(\mathbf{r})=g(\mathbf{r})-g_{eq}(r)$ calculated using NEMD simulation with the equilibrium pair potential $V_{eq}(r)$ (symbols) and equilibrium MC simulation with the nonequilibrium potential $V_{ne}(\mathbf{r})$ (solid lines) at different values of η and θ at $\gamma=0.5$ (circles), $\gamma=0.7$ (squares) and $\gamma=1.0$ (diamonds).

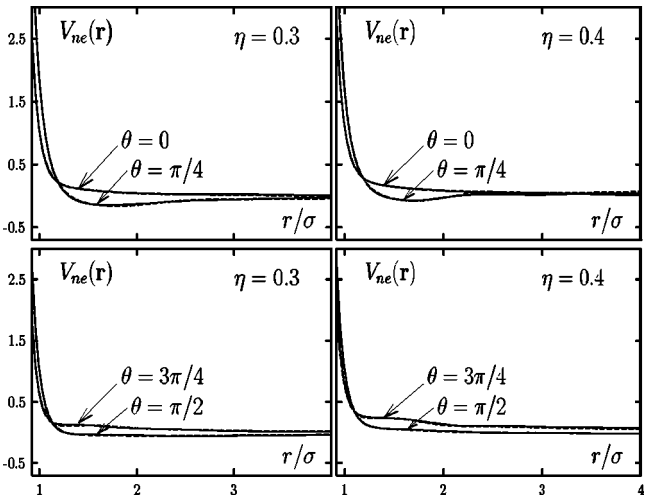

FIG. 10. Comparison of the nonequilibrium potential $V_{ne}(\mathbf{r})$ (dashed lines) and its fit (solid lines) represented by the analytical expression (A1) for different values of η and θ.

the pressure tensor (Table I). Therefore, further development of this approach is expected to provide an easy route to understanding of nonequilibrium systems. Now we turn our attention to the effect of the shear force on the liquid structure by comparing $g(\mathbf{r})$ for each angle θ as well as $g_0(r)$. As for the nonequilibrium potential, it seems more instructive to look at the difference between the nonequilibrium and equilibrium structures $\Delta g(\mathbf{r}) = g(\mathbf{r}) - g_{eq}(r)$. First of all, from a naive consideration of $g_0(r)$ as angle-averaged, one might think that $g_0(r)$ would be the same regardless of shear force. However, even $g_0(r)$ is changed under a shear field as shown in Fig. 8. As the shear rate is increased, the degree of inhomogeneity of local density in the radial direction appears higher. We point out that this result agrees with that in Ref. [20]. The results of $\Delta g(\mathbf{r})$ for $\theta = 0$, $\pi/4$, $\pi/2$, and $3\pi/4$ are shown in Fig. 9. From the figure, it is obvious, as mentioned earlier, that while the effects of shear on the liquid structure at $\theta = 0$ and $\pi/2$ are shown to be qualitatively similar, the effect at $\theta = \pi/4$ shows the opposite trend to that at $\theta = 3\pi/4$. In all cases agreement between equilibrium MC results from $V_{ne}(\mathbf{r})$ and NEMD results from the original equilibrium potential $V_{eq}(r)$ is very good.

For the sake of convenience in future applications we propose closed-form, analytical expressions for the coefficients of the expansion (7) for $V_{ne}(\mathbf{r})$ up to $|m| = 4$. These expressions together with the numerical values of the coefficients, which enter the expressions, are collected in the Appendix. We note in passing that our choice of the expressions for $V_m^{(ne)}(r)$ is purely empirical. The quality of this choice can be judged from Fig. 10, where we compare the original nonequilibrium potential $V_{ne}(\mathbf{r})$ with its fitted version for $\eta = 0.3$ and 0.4 and for $\gamma^* = 0.7$.

V. CONCLUSIONS

In this work we present and analyze the structure results for a simple, inverse-12, soft-disk fluid undergoing two-dimensional Couette flow generated by nonequilibrium molecular dynamics (NEMD). The NEMD structure has been used to extract the nonequilibrium potential, under which the structure of the equilibrium fluid coincides with that of nonequilibrium fluid. The asymptotic behavior of the "exact" nonequilibrium potential obtained in this study is substantially more long-ranged in comparison with that predicted by the theory of Gan and Eu [9,10]. Solution of the inverse problem is based on our extension of the iterative predictor-corrector method of Reatto *et al.* [17] with the corrector represented by the equilibrium MC simulation. The inversion results for structure and the pressure tensor studied converge very well to the original ones in all cases. Thus, the nonequilibrium liquid structure can be accurately reproduced via simple equilibrium simulations or theories using a properly chosen nonequilibrium potential. The method developed in the present study and numerical results presented here can be used to guide and test theoretical developments, providing them with the "experimental" results for the nonequilibrium potential.

ACKNOWLEDGMENTS

This work was supported by the Materials Sciences and Engineering Division of the U.S. Department of Energy (DOE) at Oak Ridge National Laboratory (ORNL) and through subcontract at the University of Tennessee. ORNL is operated for the DOE by UT-Battelle, LLC, under Contract No. DE-AC0500OR22725.

APPENDIX

In this appendix we present closed-form, analytical expressions for the coefficients $V_m^{(ne)}(r)$ of the expansion

$$V_{ne}(r,\theta) = \sum_{m=-4}^{4} V_m^{(ne)}(r)\exp(im\theta). \tag{A1}$$

We have

TABLE II. Numerical values of the parameters, which enter expressions (A1)–(A6).

n	a_n	b_n	α_n	β_n	$r_n^{(1)}$	$r_n^{(2)}$
0			0.602 000	3.453 747	2.78 6441	1.113 914
1	8.116 665	2.164 909	8.428 300	2.959 454		
2	6.576 726	0.485 137	4.809 397		1.942 225	
3	4.465 418	0.760 921	5.045 461	0.697 413	2.462 430	3.833 126

TABLE III. Numerical values of the density and shear rate dependent parameters, which enter expressions (A1)–(A6).

η	γ^*	n	A_n	B_n	G_n	D_n
0.30	0.5	0	1.001 714	−0.045 269	0.015 699	
		1	−149.640 854	0.367 237	0.001 221	
		2	−217.866 192	0.210 881	−0.016 889	
		3	−3.422 655	0.027 073	−0.003 455	0.000 388
0.30	0.7	0	1.003 260	−0.026 05	0.044 286	
		1	−265.889 944	0.728 840	0.012 289	
		2	−294.193 067	0.279 599	0.003 945	
		3	−6.343 483	0.051 032	−0.006 820	−0.004 279
0.35	0.5	0	1.000 470	−0.029 265	0.021 302	
		1	−105.266 736	0.298 080	−0.001 171	
		2	−203.507 542	0.224 027	−0.031 934	
		3	−2.893 122	0.021 914	−0.005 876	−0.002 419
0.35	0.7	0	1.001 231	−0.000 663	0.064 425	
		1	−184.467 440	0.572 998	0.004 936	
		2	−273.942 338	0.280 491	−0.030 932	
		3	−5.620 672	0.045 834	−0.008 189	−0.001 355
0.40	0.5	0	1.000 242	0.012 905	0.024 035	
		1	−62.104 042	0.211 616	−0.004 830	
		2	−185.341 190	0.200 982	−0.061 937	
		3	−2.381 386	0.013 401	−0.005 148 7	−0.008 116
0.40	0.7	0	1.001 740	0.086 377	0.052 047	
		1	0.007 489	2.959 454	8.428 300	
		2	−234.625 090	0.256 615	6.576 726	
		3	−0.010 505	−0.015 791	−4.515 815	0.027 540 0

$$V_0^{(ne)}(r) = \left(\frac{A_0}{r}\right)^{12} + \frac{B_0}{e^{\alpha_0(r-r_0^{(1)})}+1} + G_0 e^{-\beta_0(r-r_0^{(2)})^2}, \tag{A2}$$

$$\mathrm{Re}[V_2^{(ne)}(r)] = A_1 e^{-a_1 r} + B_1 e^{-b_1 r} + G_1 r^{\alpha_1} e^{-\beta_1 r}, \tag{A3}$$

$$\mathrm{Im}[V_2^{(ne)}(r)] = A_2 e^{-a_2 r} + B_2 e^{-b_2 r} + G_2 (r - r_2^{(1)}) e^{-\alpha_2 r}, \tag{A4}$$

$$\mathrm{Re}[V_4^{(ne)}(r)] = A_3 e^{-a_3 r} + B_3 e^{-b_3 r} + G_3 e^{-\alpha_3 (r - r_3^{(1)})^2} + D_3 e^{-\beta_3 (r - r_3^{(2)})^2}, \tag{A5}$$

$$\mathrm{Im}[V_4^{(ne)}(r)] = 0, \tag{A6}$$

and $V_{-m}^{(ne)}(r) = [V_m^{(ne)}(r)]^*$ with the asterisk denoting the complex conjugate. Numerical values for the set of the parameters a_n, b_n, α_n, β_n, $r_n^{(1)}$ and $r_n^{(2)}$ are collected in Table II and for the set of parameters A_n, B_n, G_n and D_n are collected in Table III. The latter set of parameters depends on the packing fraction η and shear rate γ^*.

[1] D. Ronis, Phys. Rev. Lett. **52**, 473 (1984).
[2] T. P. C. van Noije, M. H. Ernst, R. Brito, and J. A. G. Orza, Phys. Rev. Lett. **79**, 411 (1997).
[3] T. P. C. van Noije, M. H. Ernst, and R. Brito, Phys. Rev. E **57**, R4891 (1998).
[4] J. C. Rainwater and S. Hess, Physica A **118**, 371 (1983).
[5] S. Hess, J. Phys. (Paris) **46**, C3 (1985).
[6] J. F. Lutsko, Phys. Rev. Lett. **86**, 3344 (2001).
[7] J. F. Lutsko, Phys. Rev. Lett. **77**, 2225 (1996).
[8] E. Waisman, Mol. Phys. **25**, 45 (1973).
[9] H. H. Gan and B. C. Eu, Phys. Rev. A **45**, 3670 (1992).
[10] H. H. Gan and B. C. Eu, Phys. Rev. A **46**, 6344 (1992).
[11] Yu. V. Kalyuzhnyi, S. T. Cui, P. T. Cummings, and H. D. Cochran, Phys. Rev. E **60**, 1716 (1999).
[12] Yu. V. Kalyuzhnyi, S. T. Cui, and H. D. Cochran, Phys. Rev. E **63**, 011209 (2000).
[13] D. J. Evans and G. P. Morriss, *Statistical Mechanics of Nonequilibrium Liquids* (Academic, New York, 1990).

[14] S. Nose, Mol. Phys. **52**, 255 (1984).
[15] S. Nose, J. Chem. Phys. **81**, 511 (1984).
[16] W. G. Hoover, Phys. Rev. A **31**, 1695 (1985).
[17] L. Reatto, D. Levesque, and J. J. Weis, Phys. Rev. A **33**, 3451 (1986).
[18] D. A. Ward and F. Lado, Mol. Phys. **63**, 623 (1988).
[19] J. D. Talman, J. Comput. Phys. **29**, 35 (1978).
[20] H. J. M. Hanley, G. P. Morriss, T. R. Welberry, and D. J. Evans, Physica A **149**, 406 (1988).